Modeling Water-Steam Flow in Fractured Reservoirs: Application to Enhanced Geothermal Systems

Shuang Zheng[1] and Mukul M. Sharma[1]

[1]The University of Texas at Austin.

Corresponding author: Mukul M. Sharma (msharma@mail.utexas.edu)

Key Points:

- A water-steam two-phase fractured geothermal reservoir simulator with coupled flow and thermal processes is developed.
- The simulator is used to demonstrate the effect of fracture spacing, well spacing, injection rate, etc. in an enhanced geothermal system.
- Heat conduction is the main contributor to the heat flux while convective flow does not contribute much in enhanced geothermal systems.

Abstract

A water-steam two-phase fractured geothermal reservoir model is presented in this paper. Coupled flow and thermal processes are solved in the reservoir and fractures using the pressure-enthalpy formulation and water-steam phase behavior correlations. Both an implicit pressure, explicit enthalpy and a fully implicit solution algorithm have been developed. After model validation, this simulator is used to model the heat extraction rate from enhanced geothermal systems (EGS). The temperature and energy flux from the production well are plotted and analyzed. The effects of several key parameters on enhanced geothermal systems are investigated. It is found that injection rate, fracture spacing, well spacing, and effective fracture surface area have the biggest impact on the heat extraction rate. It is also found that heat conduction is the main contributor to the heat flux while convective fluid flow does not contribute much when the reservoir permeability i.e., the rate of gravity driven convection is low. The heat flux from the earth does not affect short-term EGS production but can be an important factor for long-term EGS development. The geothermal reservoir simulator presented in this paper can be used to optimize and design EGS in geothermal fields (fracture spacing, well spacing, injection rate, etc.).

1 Introduction

Geothermal energy has recently gained much more attention with the global trend of energy transition to green energy and net zero emission goals within the twenty-first century. One major advantage of geothermal energy is that the utilization of the underground heat flow does not produce carbon emissions, and it can reduce greenhouse gas emissions by at least 90% as compared to oil or gas production (Glassley, 2014). Other key benefits of geothermal energy include, (a) it is renewable, (b) it is available 24 hours a day and provides baseload power, (c) it does not need expensive energy storage, and (d) it has a small footprint. Geothermal energy can be classified by temperature or by depth. Shallow or lower temperature sources (0-1 km or less than 100 °C), intermediate resources (1-4 km, or less than 200 °C), and deep / hot resources (typically 4 km to 6 km with temperatures of 200 °C or hotter). The shallow resources are good for direct use such as heating and cooling whereas the high temperature resources can be used for electricity generation (Johnston et al., 2011). There are many instances where geothermal gradients are very high and high temperatures can be achieved at relatively shallow depth. Such locations are preferred sites for geothermal operations.

Geothermal reservoirs can be developed either via circulation of injected fluids or through the direct production of the subsurface fluids from the reservoir. There are two primary methods used to extract the heat from the subsurface. Enhanced Geothermal Systems (EGS) in which water is injected into the wellbore, flows through hydraulic and natural fractures, is heated-up by the geothermal reservoir, and produced from another wellbore with the extracted geothermal energy. On the other hand, in a closed loop geothermal system, a working fluid (such as water or CO_2) is circulated within a wellbore in a continuous loop with no direct contact with the reservoir fluid. Heat exchange mainly happens by conduction into the wellbore. No fractures are created. This paper deals only with Enhanced Geothermal Systems.

Enhanced Geothermal Systems use hydraulically fractured wells to extract heat from the earth. As shown in Figure 1, in the creation of an enhanced geothermal system, wells are traditionally drilled in dry hot rocks and then stimulated by hydraulic fracturing to create

fractures connecting the injection and production wellbores. Water or other working fluids such as CO_2 at ambient surface temperature are pumped into the injection wellbore. The fluid heats up as it circulates through the fractures until it is produced from the production wellbore. The high temperature working fluid (usually water or steam) is sent to a power generator to generate electricity and the cooled working fluid is injected back into the injection well to be re-heated.

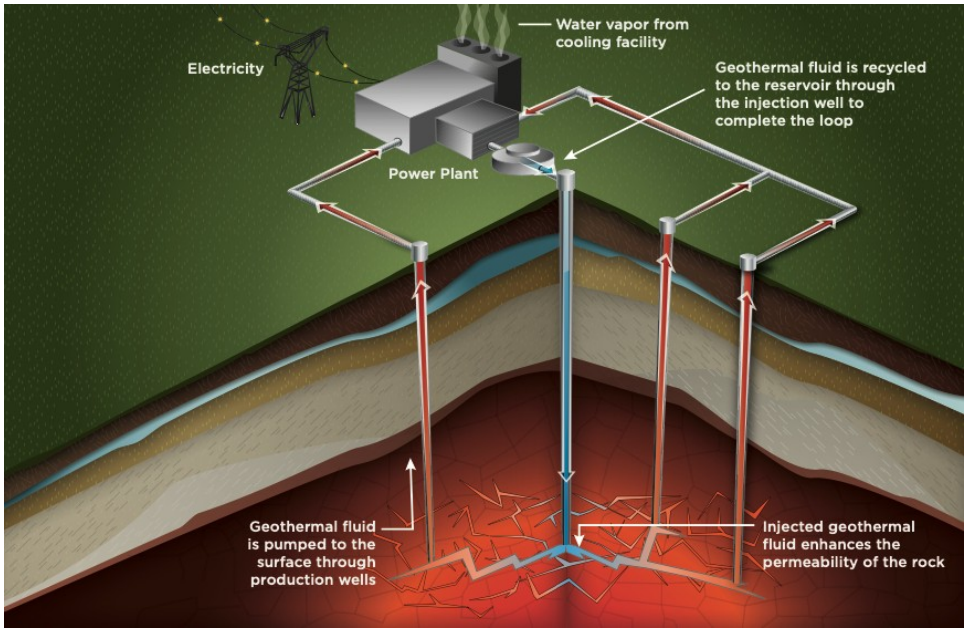

Figure 1. Illustration of enhanced geothermal systems (U.S. Department of Energy).

Modeling can play a key role in designing, assessing, developing, and managing geothermal reservoirs. Geothermal reservoir modeling shares similarities to modeling oil and gas reservoirs (Kennedy et al., 2010). Geothermal reservoir simulation involves the solution of highly nonlinear, coupled equations for flow and heat transport in heterogeneous reservoirs with fractures. The results from reservoir modeling can assist engineers and executives in the decision-making process. A few geothermal reservoir simulation codes have been developed in the past several decades. The first generation of geothermal reservoir models was developed in the 1970s (Mercer & Pinder, 1973; Coats, 1977; Donaldson & Sorey, 1979; Faust & Mercer, 1979). The DOE Geothermal Program sponsored development of geothermal reservoir simulators including SHAFT, MULKOM, TETRAD, and the TOUGH family of codes (Kennedy et al., 2010). More recently, a geothermal reservoir simulator has been developed in an automatic differentiation reservoir simulation framework (Wong, 2018).

The objective of this paper is to present a two-phase geothermal reservoir model that can be used to simulate enhanced geothermal systems with vertical or horizontal wells with multiple hydraulic and natural fractures. The model includes geomechanical effects, poro-thermo-elasticity, thermal convection/conduction, water-steam phase behavior as well as flow in complex fracture networks and in the rock matrix. Based on the model we have developed we quantify the key parameters that affect the performance of enhanced geothermal systems. The model formulation including governing equations and water-steam phase behavior modeling is discussed in Section 2. Models for water-steam phase behavior are discussed in Section 3.

Numerical methods, solution algorithms and model implementation are discussed in Section 4. The newly developed model is validated against two problems with analytical solutions in Section 5. The Base Case setup and results are presented in Section 6 and parametric studies are presented in Section 7. Key conclusions are summarized in Section 8.

2 Model Formulation

We follow the work by Faust & Mercer (1979) in the derivation of the geothermal reservoir simulation formulation. The following assumptions are made in the derivation:

1) Two-phase (water, steam) flow and phase behavior,
2) Flow in the rock matrix is described by Darcy's law while considering gravity,
3) Capillary pressure is neglected,
4) The pressure-volume work is ignored, which means that the internal energy is equal to the enthalpy.

2.1 Mass conservation equation

The mass conservation equations for the water phase and steam phase are shown in Eq. (1) and Eq. (2),

$$\frac{\partial\left(\phi S_w \rho_w\right)}{\partial t}+\nabla\cdot\left(\rho_w u_w\right)-\frac{\rho_w q_w}{V}+d_v=0 \tag{1}$$

$$\frac{\partial\left(\phi S_s \rho_s\right)}{\partial t}+\nabla\cdot\left(\rho_s u_s\right)-\frac{\rho_s q_s}{V}-d_v=0 \tag{2}$$

where ϕ is the porosity, S_w and S_s are the water and steam saturation, ρ_w and ρ_s are the water and steam density, q_w and q_s are the volumetric source term for water and steam. d_v is the mass transfer term between the water phase and steam phase. V is the cell volume. u_w and u_s are the Darcy velocity of water and steam phase and can be calculated using Eq. (3) and Eq. (4).

$$u_w=\frac{-k\,k_{rw}}{\mu_w}\nabla\left(p-\rho_w g D\right) \tag{3}$$

$$u_s=\frac{-k\,k_{rs}}{\mu_s}\nabla\left(p-\rho_s g D\right) \tag{4}$$

where k is the matrix or fracture permeability, p is the pressure, g is the gravity constant, D is the depth, k_{rw} and k_{rs} are the relative permeability of water and steam phase, μ_w and μ_s are the viscosity of the water and steam phase.

2.2 Pressure equation

The pressure equation is derived by adding the mass conservation equation (1) and (2), as shown in Eq. (5) and in a compact form as shown in Eq. (6),

$$\frac{\partial\left(\phi S_s \rho_s+\phi S_w \rho_w\right)}{\partial t}+\nabla\cdot\left(\rho_s u_s\right)+\nabla\cdot\left(\rho_w u_w\right)-\frac{\rho_s q_s}{V}-\frac{\rho_w q_w}{V}=0 \tag{5}$$

$$\sum_{i=1}^{2}\frac{\partial(\phi S_i\rho_i)}{\partial t}+\sum_{i=1}^{2}\nabla\cdot(\rho_i u_i)-\sum_{i=1}^{2}\frac{\rho_i q_i}{V}=0 \tag{6}$$

Substituting Eq. (3) and Eq. (4) into Eq. (6), the final form of the pressure equation (7) is obtained.

$$\sum_{i=1}^{2}\frac{\partial(\phi S_i\rho_i)}{\partial t}-\sum_{i=1}^{2}\nabla\cdot\left[\rho_i\frac{k\,k_{ri}}{\mu_i}\nabla(p-\rho_i gD)\right]-\sum_{i=1}^{2}\frac{\rho_i q_i}{V}=0 \tag{7}$$

where S_i, ρ_i, u_i, q_i, k_{ri}, μ_i are the saturation, density, Darcy velocity, volumetric source term, relative permeability, and viscosity of phase i.

2.3 Enthalpy equation

The enthalpy equation is derived as a conservation of energy and is shown in Eq. (8).

$$\frac{\partial}{\partial t}\left[(1-\phi)\rho_r U_r+\phi\sum_{i=1}^{2}\rho_i U_i S_i\right]-\nabla\cdot(K\nabla T)+\sum_{i=1}^{2}\nabla\cdot(\rho_i h_i u_i)-\sum_{i=1}^{2}\frac{\rho_i q_i h_i}{V}=0 \tag{8}$$

where ρ_r and U_r are the density and specific internal energy of the rock. U_i and h_i are the specific internal energy and specific enthalpy of phase i. K is the bulk thermal conductivity calculated by Eq. (9),

$$K=\phi\sum_{i=1}^{2}k_i S_i+(1-\phi)k_s \tag{9}$$

where k_i and k_s are the thermal conductivity of phase i and solid (rock). Eq. (10) is obtained by substituting Eq. (3) and Eq. (4) into Eq. (9).

$$\frac{\partial}{\partial t}\left[(1-\phi)\rho_r U_r+\phi\sum_{i=1}^{2}\rho_i U_i S_i\right]-\nabla\cdot(K\nabla T)-\sum_{i=1}^{2}\nabla\cdot\left[\rho_i h_i\frac{k\,k_{ri}}{\mu_i}\nabla(p-\rho \tag{10}$$

Using assumption 4), the specific internal energy is replaced by the specific enthalpy and the final form of the enthalpy equation (11) is obtained,

$$\frac{\partial}{\partial t}\left[(1-\phi)\rho_r h_r+\phi\sum_{i=1}^{2}\rho_i h_i S_i\right]-\nabla\cdot(K\nabla T)-\sum_{i=1}^{2}\nabla\cdot\left[\rho_i h_i\frac{k\,k_{ri}}{\mu_i}\nabla(p-\rho_i g \tag{11}$$

3 Water-Steam Phase Behavior Modeling

In this work, the water-steam phase behavior is modeled using the correlations presented by O'Sullivan (1981). The specific enthalpy, density, temperature, and viscosity of water and steam phases are modeled as functions of pressure and enthalpy.

3.1 Specific Enthalpy of Saturated Phase

The specific enthalpy of saturated water and saturated steam can be calculated as a function of pressure using Eq. (12) and Eq. (13).

$$h_{ws}=10^{-4}\left(7.30984\times10^{9}+12.9239\,p-1.00333\times10^{-8}p^{2}+3.9881\times10\right. \tag{12}$$

$$h_{ss}=10^{-4}\left(2.82282\times10^{10}-3.91952\times10^{6}p^{-1}+2.54342\times10^{23}p^{-2}-9.\right. \tag{13}$$

where h_{ws} and h_{ss} are the specific enthalpy of the saturated water phase and saturated steam phase.

3.2 Density

The density for single-phase compressed water and single-phase superheated steam can be calculated as a function of pressure and enthalpy as shown in Eq. (14) and Eq. (15).

$$\rho_w = 10^3\left(1.00207 + 4.42607\times10^{-12}\,p - 5.47456\times10^{-16}\,h + 5.02875\times 1\right. \quad (14)$$

$$\rho_s = 10^3\left(-2.26162\times10^{-5} + 4.38441\times10^{-10}\,p - 1.79088\times10^{-24}\,ph + 3.\right. \quad (15)$$

The density of the two-phase fluid mixture is calculated by a volumetric average of the water and steam density as shown in Eq. (16).

$$\rho = S_w\rho_w + S_s\rho_s \quad (16)$$

3.3 Temperature

The temperature for single-phase compressed water can be calculated using Eq. (17).

$$T = 273.15 - 2.41231 + 2.56222\times10^{-12}\,h - 9.31415\times10^{-19}\,p^2 - 2.256 \quad (17)$$

The temperature for single-phase superheated steam can be calculated using Eq. (18).

$$T = 273.15 - 374.669 + 4.79921\times10^{-7}\,p - 6.33606\times10^{-17}\,p^2 + 7.3938 \quad (18)$$

In the two-phase region, the temperature is calculated using Eq. (17) with the saturated water enthalpy h_{ws}, because temperature does not change during a phase change, as shown in Eq. (19).

$$T = 273.15 - 2.41231 + 2.56222\times10^{-12}\,h_{ws} - 9.31415\times10^{-19}\,p^2 - 2.25 \quad (19)$$

The phase heat capacity $\frac{dH}{dT}$ can be back calculated from Eq. (17), (18), and (19).

3.4 Viscosity

The viscosity of the water and steam is a function of the temperature and is calculated as shown in Eq. (20) and Eq. (21).

$$\mu_w = 10^{-7}\left[241.4\times10^{\frac{247.8}{|T-273.15|+133.15}}\right] \quad (20)$$

$$\mu_s = 10^{-7}\left[0.407\left(T-273.15\right)+80.04\right] \quad (21)$$

3.5 Rock enthalpy

The specific enthalpy of the rock matrix is calculated by Eq. (22).

$$\Delta h_r = C_{pr}\Delta T \quad (22)$$

where C_{pr} is the heat capacity of the rock.

3.6 Saturation

In the simulation, a control volume may be single phase water ($S_w = 1$), single phase steam ($S_w = 0$), or a water-steam two phase mixture ($0 < S_w < 1$).

If the calculated enthalpy is lower than the saturated water phase enthalpy, the control volume contains single phase water. If the calculated enthalpy is greater than the saturated steam phase enthalpy, the control volume is single phase steam. If the calculated enthalpy is between the saturated water phase enthalpy and saturated steam phase enthalpy, the control volume contains both phases. The enthalpy of the two-phase fluid mixture is defined by Eq. (23).

$$h = \frac{S_w \rho_w h_w + S_s \rho_s h_s}{\rho} \tag{23}$$

After some algebra, the water saturation for a two-phase state control volume can be derived from Eq. (16) and Eq. (23) as shown in Eq. (24).

$$S_w = \frac{\rho_{ss}\left(h_{ss} - h\right)}{h\left(\rho_{ws} - \rho_{ss}\right) - \left(h_{ws}\rho_{ws} - h_{ss}\rho_{ss}\right)} \tag{24}$$

where ρ_{ws} and ρ_{ss} are the saturated phase density of water and steam calculated using the current control volume pressure and the saturated phase specific enthalpy calculated from the current control volume pressure. The steam saturation is calculated using Eq. (25).

$$S_s = 1 - S_w \tag{25}$$

4 Numerical Methods, Solution Algorithms and Model Implementation

Two formulations, a pressure-saturation-temperature formulation and a pressure-enthalpy formulation have been compared in the past (Wong, 2018). In this work, we implement and use the pressure-enthalpy formulation into our previously developed, fully-integrated simulation framework (Zheng & Sharma, 2020). Pressure and enthalpy equations are solved with either an implicit pressure, explicit enthalpy option or a fully implicit option. Finite volume methods are used for space discretization. Pressure and specific enthalpy are selected as the primary unknowns.

4.1 Finite volume discretization

The pressure and enthalpy equations are solved for the pressure and specific enthalpy distribution in the reservoir and fracture domains. The temperature and saturation distributions are updated based on the converged solution of pressure and enthalpy using Eq. (17), (18), (19) and Eq. (24), (25). The finite volume method is used to discretize the equations in the reservoir domain and the fracture domain. The detailed discretizations are summarized in Appendix A.

4.2 Implicit pressure, explicit enthalpy algorithm

The implicit pressure, explicit enthalpy solution enthalpy algorithm is shown in Figure 2(a). For each time step, the pressure equation in the reservoir domain and/or fracture domain are solved first followed by the solution of the enthalpy equation in the reservoir domain and/or fracture domain. Then the saturation in each control volume is updated as discussed in Section 3.6. The temperature is then updated based on the saturation state and correlations presented in Section 3.3.

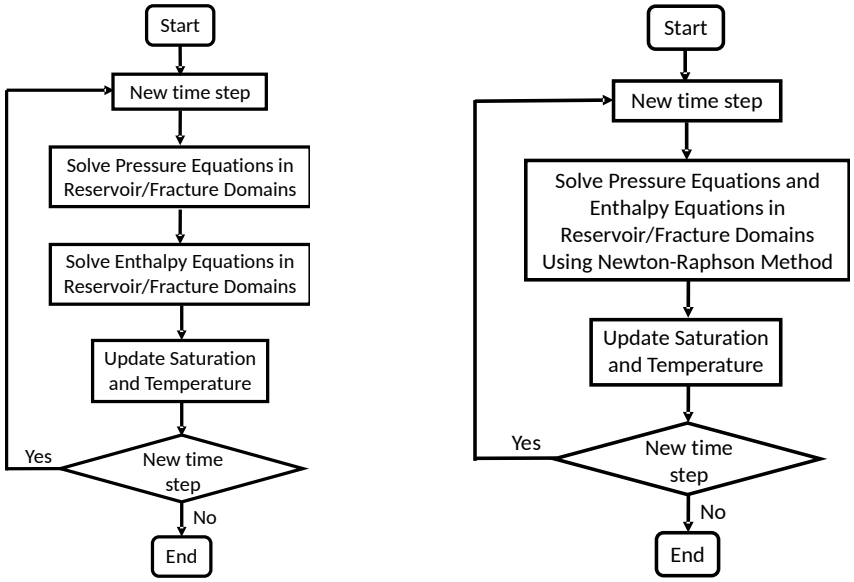

Figure 2. Solution algorithms for our geothermal reservoir simulator. **a.** Implicit pressure, explicit enthalpy algorithm. **b.** Fully implicit algorithm.

4.3 Fully implicit algorithm

The fully implicit solution algorithm is shown in Figure 2(b). For each time step, the pressure equation and enthalpy equation within the reservoir domain and/or fracture domain are solved using the Newton-Raphson method. The saturation in each control volume is updated as discussed in Section 3.6. Finally, the temperature is updated based on the saturation state and correlations in Section 3.3.

4.4 Model implementation

The simulator is written in a modular structure using C++. The simulator is written to be fully parallelized using Message Passing Interface (MPI). The foam-extend-3.2 package (Weller et al., 1998) is used for meshing and data structure, etc. The Trilinos project is used to for linear algebra. Epetra and Tpetra packages (Baker & Heroux, 2012) are used to store distributed matrix and vector objects. AztecOO and Belos parallelized iterative solver (GMRES) (Heroux, 2004; Bavier et al., 2012) and Ifpack2 preconditioner (ILUT) (Prokopenko et al., 2016) are used to solve the linear system from the Newton-Raphson method. Amesos2 (Bavier et al., 2012) is used as the parallelized direct solver interface package to direct solvers. More details can be found in Zheng et al. (2019) and Zheng & Sharma (2020).

5 Model Validation

In this section, we validate the model with two problems with known analytical solutions. The one-dimensional advection-diffusion problem and the radial flow problem are used validate the flow and thermal functionalities in the model.

5.1 1-D advection-diffusion problem

We validate the coupled pressure and enthalpy equations against the one-dimensional advection-diffusion equation. The analytical solution to the advection-diffusion equation has been presented in Zheng et al. (2020).

To compare our numerical model with an analytical solution, we set up a 1-D case with one rate-constrained injector on the first cell and one pressure-constrained producer on the last cell. The parameters are shown in Table 1. The mesh, the pressure distribution, and the temperature distribution at the final time step are shown in Figure 3. Figure 4 shows the simulated dimensionless temperature profile versus dimensionless length plot against the analytical solution at 100, 300, and 500 days. The numerical results match very well with the analytical solution.

Table 1. *Input parameters for the validation with 1-D advection-diffusion equation*

Parameter	Value	Unit
Domain dimension	$200 \times 4 \times 4$	m^3
Number of grids	$500 \times 1 \times 1$	
Porosity	0.2	
Permeability	1e-13	m^2
Rock density	2650	kg/m^3
Rock specific heat capacity	1000	$J/(K \cdot kg)$
Rock thermal conductivity	1.7	$W/(m \cdot K)$
Water/steam thermal conductivity	0.58	$W/(m \cdot K)$
Initial temperature	310	K
Injection temperature	370	K
Injection rate	0.00004	m^3/s
Production pressure	13.1	MPa
Initial pressure	13.78952	MPa
Simulation time	43200000	s

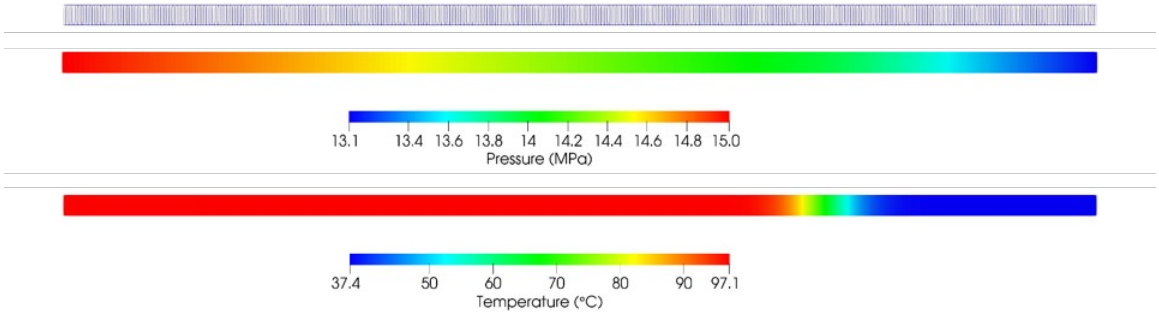

Figure 3. Mesh with grids, final pressure distribution, and final temperature distribution for the 1-D advection-diffusion validation case.

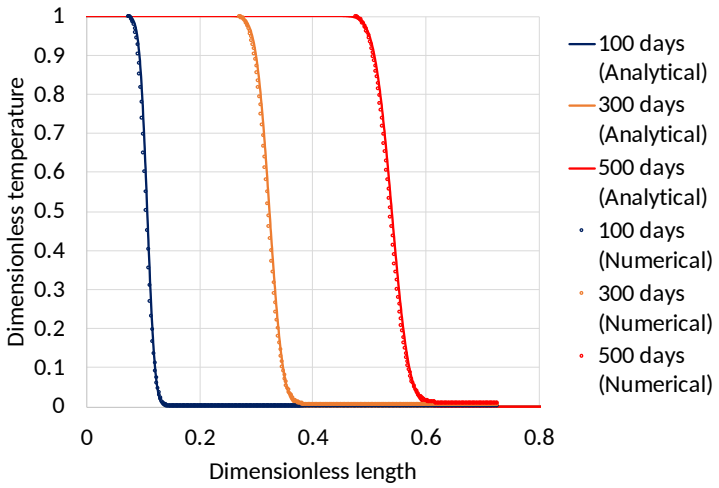

Figure 4. Comparison of the dimensionless temperature distribution between numerical solution and analytical solution at selected time steps for the 1-D advection-diffusion validation case.

5.2 Radial heat transport problem

In the second validation case, we simulate a radial heat transport problem. The radial heat transport can be described by the radial heat convection-conduction equation. The analytical solution to the radial heat convection-conduction equation is given by Ross et al. (1982)

To validate the numerical model with the analytical solution to the radial heat transport problem, we setup a radial mesh as shown in Figure 5. The inner diameter is set to 1 meter whereas the outer diameter is set to 2000 meters. The number of grids in the radial direction and circumferential direction is set to 500 and 40, respectively. A Peaceman well model is used in the inner radial boundary to inject cold water at a rate of $0.01\,m^3/s$. The pressure at the outer radial boundary is fixed at $5\,MPa$. The total simulation time is set to $3\times10^9\,s$. Other key parameters are listed in Table 2.

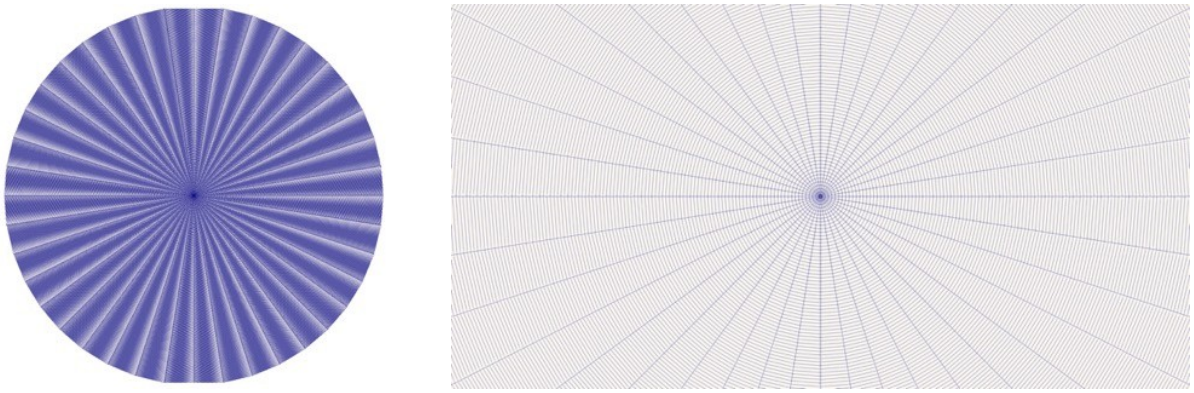

a **b**

Figure 5. Mesh for the radial flow validation case. **a.** The entire computation domain. **b.** A zoomed-in view of the mesh.

Table 2. *Input Parameters for the Validation with Radial Flow Analytical Solution*

Parameter	Value	Unit
Inner diameter	1	m
Outer diameter	2000	m
Number of grid in radial direction	500	
Number of grid circumferential direction	40	
Rock density	2500	kg/m^3
Rock specific heat capacity	1000	$J/(K \cdot kg)$
Rock thermal conductivity	2.5	$W/(m \cdot K)$
Water/steam thermal conductivity	2	$W/(m \cdot K)$
Porosity	0.2	
Permeability	1e-12	m^2
Injection rate	0.01	m^3/s
Injection temperature	433.15	K
Outer boundary pressure	5	MPa
Initial pressure	5	MPa
Initial temperature	444.15	K
Simulation time	3e9	s

Figure 6 depicts the pressure and temperature distribution at the end of the simulation. The temperature along the radial direction at simulation times of $1 \times 10^9 s$, $2 \times 10^9 s$, and $3 \times 10^9 s$ are plotted and compared with the analytical solution in Figure 7. A good match between the numerical solution and analytical solution is clearly observed. The small mismatch is caused by the fact that in the numerical model, the heat capacity and density of water change both in space and in time while in the analytical solution, only a single value of heat capacity and density of water can be specified.

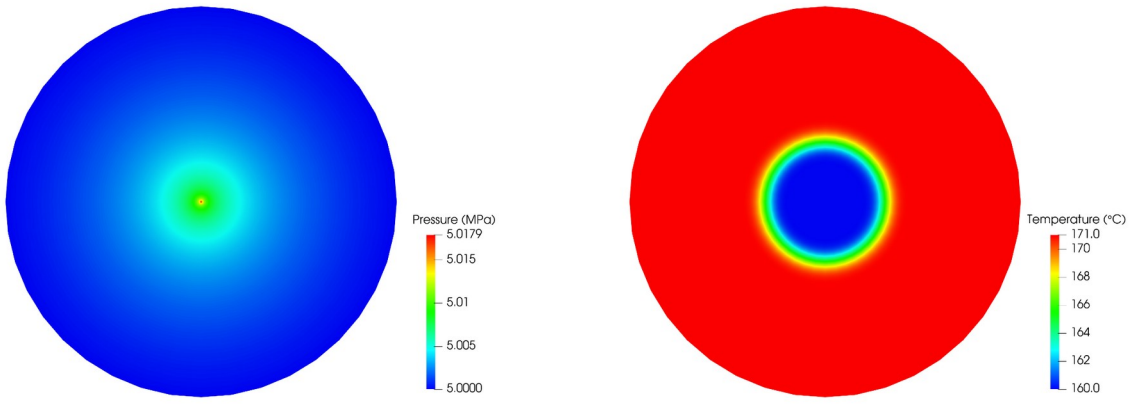

a **b**

Figure 6. Results for the radial flow validation case. **a.** Pressure distribution. **b.** Temperature distribution.

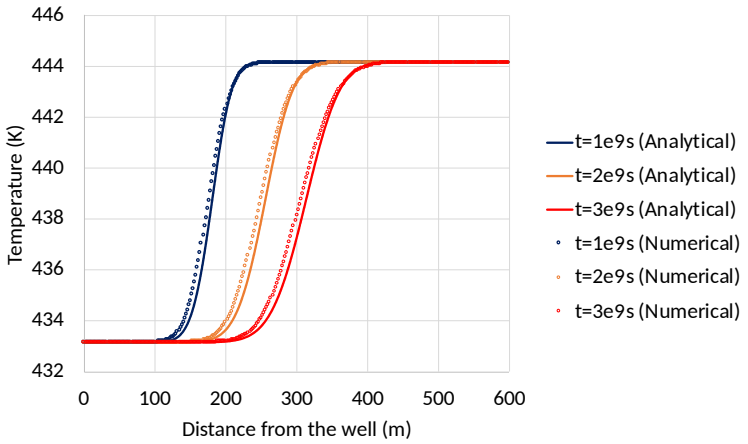

Figure 7. Comparison of temperature radial distribution between numerical and analytical solutions at three selected time steps for the radial flow validation case.

6 Base Case Setup and Results

6.1 Base Case setup

In this section, we discuss the Base Case setup for a sector model for an idealized enhanced geothermal system. The results from the Base Case are then used to perform a parametric study to clearly show the impact of different system variables on the performance of enhanced geothermal systems.

Figure 8 shows a schematic plot of an ideal enhanced geothermal system in which the injection wells and production wells are drilled between each other. The injection wells are hydraulically fractured, and the planar fractures connect the two production wells on both sides of the injection well. We recognize that the fracture network in the field can be much more complex, however, we have chosen this simplified EGS geometry deliberately so that the results can be more easily understood and interpreted. The simplified fracture network is symmetric, and a sector model can be used to represent the whole system and results can be scaled up to the whole system. Although we have the modeling capability to simulate the entire region between wells and incorporate much more complex fracture networks, using the symmetry of the problem reduces the computation time significantly. A much smaller number of grids can be used in the sector model at a higher spatial resolution. The simpler geometry also helps us better understand the factors that control the performance of the enhanced geothermal system by conducting parametric studies. The simulated sector model is shown within the orange box in Figure 8.

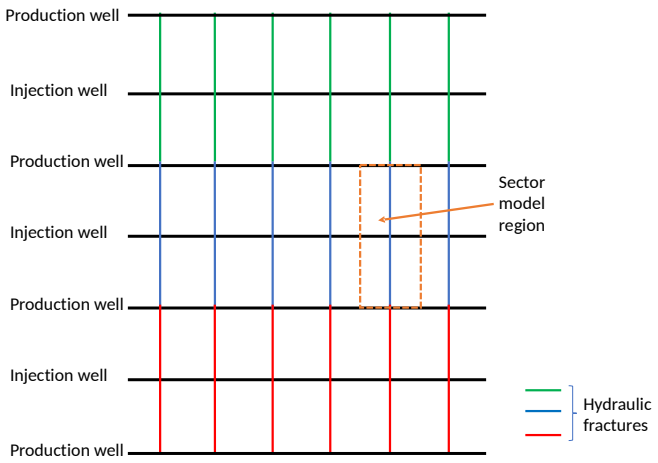

Figure 8. Schematic plot of enhanced geothermal systems with alternating injection and production wells. The sector that is modeled is shown in the orange box.

The reservoir mesh for the Base Case sector model is shown in Figure 9(a) with two cylinders representing the injection and production wellbores. The sector model has a size of 20 meters in the direction along the wellbore, 200 meters in the direction perpendicular to the wellbore (well spacing), and 100 meters in the vertical (height) direction. The number of cells in the three directions are 16, 40, and 20, respectively, leading to a uniform cell size of $16 \times 5 \times 5\, m^3$. A single fracture connecting the injection and production wellbores exists in the middle of the sector model with a fracture height of 50 meters and fracture length of 200 meters. The discretization of the fracture surface follows the discretization of the reservoir mesh, which gives a discretized fracture control area of $5 \times 5\, m^2$. The fracture width is assumed to be $2\, mm$. It is worth noting that this sector model can be used to simulate both horizontal and vertical well pairs.

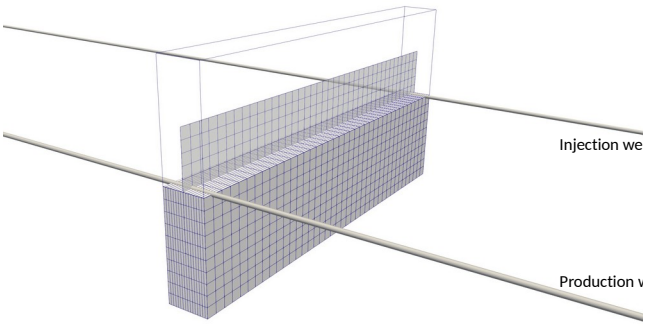

a

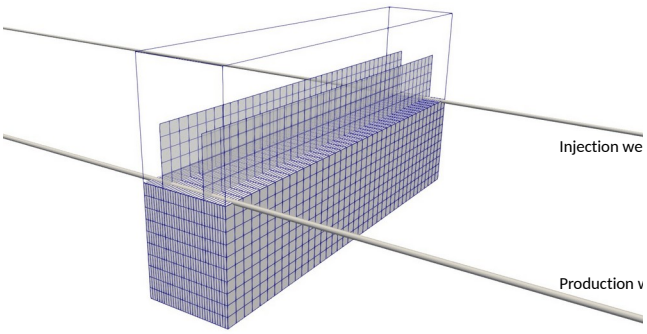

b

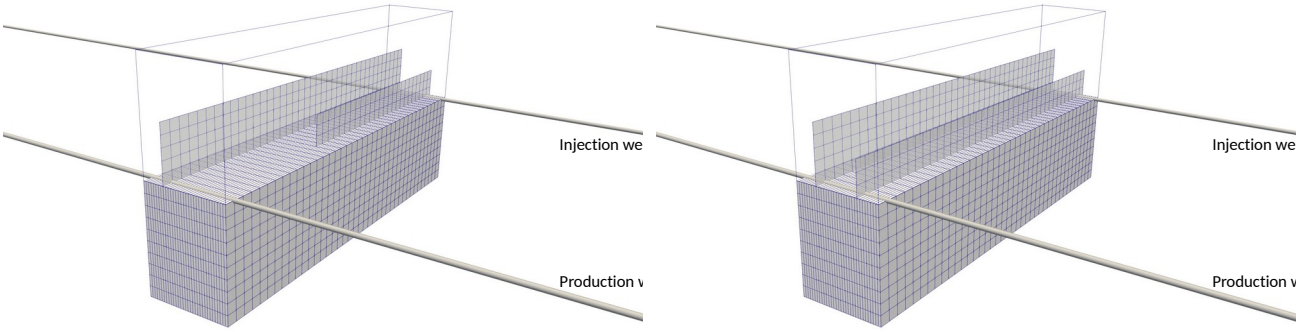

c **d**

Figure 9. Meshes used in the simulation study. **a.** Mesh for the sector model in the Base Case. The bottom half of the reservoir mesh and the top half of the fracture mesh are shown. The two cylinders represents one injection well and one production well. **b.** Mesh used for two uniform fractures. **c.** Mesh used for the failed fracture connection case. **d.** Mesh used for a case where the fracture surface area in doubled and a thief fracture is present.

In the Base Case, the original reservoir pressure is set to 40 MPa and the original reservoir temperature is set to 200 $°C$. The injection well is set to have an injection rate of 1000 barrels per day per fracture. Cold water with a temperature of 30 $°C$ is injected. The production well is set to have a bottom hole pressure of 39 MPa. The total simulation time is set to 5 years. Straight-line relative permeability curves with no residual saturations are chosen for the fracture. This means that the phase relative permeability is equal to the phase saturation. Other input parameters are listed in Table 3. No flow and no thermal flux boundary conditions are applied to the six outer boundaries of the sector model in the Base Case.

Table 3. *Input Parameters for the Base Case*

Parameter	Value	Unit
Reservoir mesh size	$20 \times 200 \times 100$	m^3
Reservoir mesh discretization	$16 \times 40 \times 20$	
Fracture length	200	m
Fracture height	50	m
Rock density	2057	kg/m^3
Rock specific heat capacity	1000	$J/(K \cdot kg)$
Rock thermal conductivity	2.5	$W/(m \cdot K)$
Water/steam thermal conductivity	0.5	$W/(m \cdot K)$
Initial pressure	40	MPa
Initial temperature	200	$°C$
Injection temperature	30	$°C$
Porosity	0.1	
Reservoir permeability	1e-18	m^2
Fracture permeability	1e-8	m^2
Fracture width	2	mm

Injection rate	1000	*bpd*
Production pressure	39	*MPa*

6.2 Base Case results

The temperature distributions in the reservoir after 1, 2, 3, 4, and 5 years of injection-production are shown in Figure 10. The reservoir rock volume near the fracture cools down faster than the top and bottom part of the reservoir (the region without a penetrating fracture). The reservoir rock near the injection well cools down faster than the reservoir rock near the production well. As the injection proceeds, the temperature in the top (overburden) and bottom confining layers also decreases slowly, primarily by conduction.

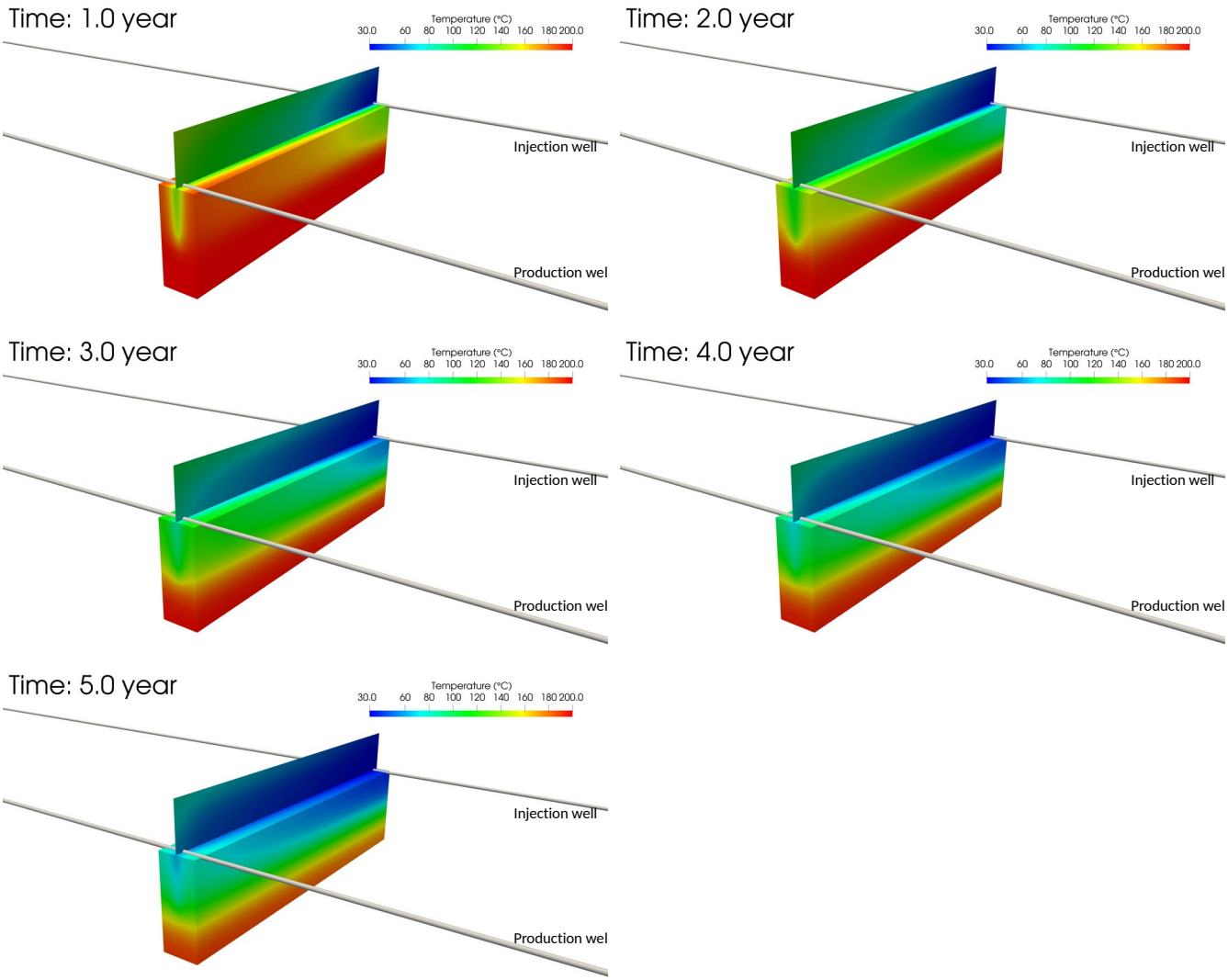

Figure 10. Temperature distribution in the reservoir after one, two, three, four, and five years operation in the Base Case.

The temperature distributions in the fracture after 1, 2, 3, 4, and 5 years of fluid circulation are shown in Figure 11. As expected, the temperature near the production well (right side) is the lowest and the water is heated by thermal conduction as it travels towards the production well. However, the heat extraction rate decreases with time as the reservoir temperature cools down and less heat can be transferred to the water in the fracture from the reservoir. The produced water temperature also decreases with time. After 5 years of production, the injected water can no longer be heated up effectively under the conditions set up for the Base Case.

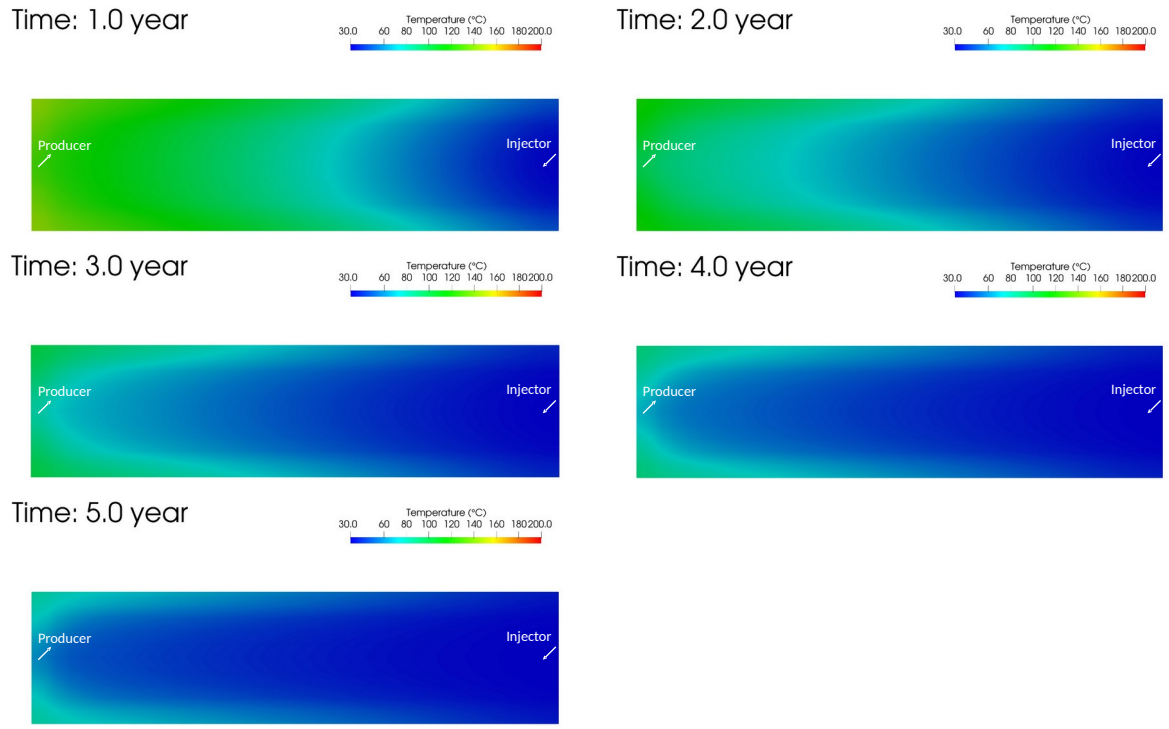

Figure 11. Temperature distribution in the fracture after one, two, three, four, and five years of operation for the Base Case.

The temperature distribution in the fracture at selected time steps is plotted in Figure 12(a). As expected, the temperature is the highest at the production wellbore and the lowest at the injection wellbore. The temperature in the fracture decreases with time. At the production wellbore, the temperature after one-year production is about $126\,°C$ and decreases to about $100\,°C$ after two years of production. After five years of production, the temperature is about $60\,°C$. Higher injection rates result in a faster decrease in temperature with time.

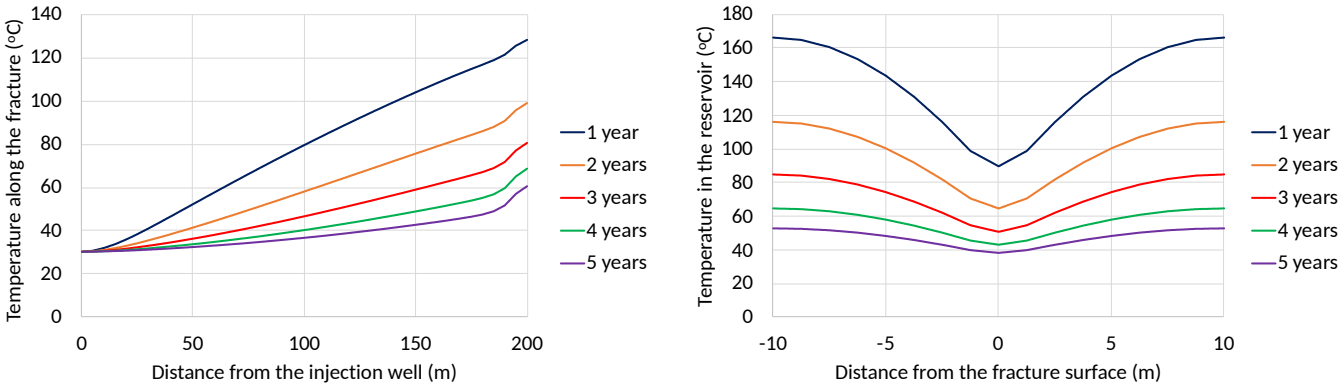

a **b**

Figure 12. Temperature distribution at different injection time for the Base Case. **a.** The temperature distribution inside and along the middle of the fracture. **b.** The temperature distribution inside the reservoir (half-way from the injector and producer) perpendicular to the fracture surface.

The temperature distribution perpendicular to the fracture surface in the reservoir between the two wells is shown in Figure 12(b). The fracture is located where the distance from the fracture surface is zero and the temperature distribution is symmetric on both sides of the fracture. We can observe that the temperature is the lowest near the fracture surface and the highest at the outer boundary. The temperature decreases drastically in the first year, but the rate of decrease slows down over time.

7 Parametric Study

In this section, we conduct a systematic study to investigate the impact of some important factors that affect the efficiency of an enhanced geothermal system. The effects of injection rate, fracture spacing, well spacing, rock permeability, thermal boundary condition, and non-uniform fluid injection (including fracture permeability, fracture width, fracture dimension, well-to-well connectivity) are studied. Production well temperature and net energy flux into the injected fluid versus time are plotted and analyzed.

7.1 Effect of injection rate

In the first parametric study, we show the effect of injection rate on geothermal energy extraction rate. Six simulation cases are run with the injection rate varying from 100 to 1000 (Base Case) to 10000 barrels per day (bpd) per fracture. The production temperature versus time for different injection rates is plotted in Figure 13(a). The net energy flux is calculated by subtracting the injected water enthalpy from the produced water enthalpy and is shown in Figure 13(b). The net energy flux per unit fracture surface area is also plotted in Figure 13(b). Since in this set of runs, the fracture surface area for different cases is the same ($20000\,m^2$), the curves for net energy flux versus time and net energy flux per unit fracture surface area versus time are identical and overlap.

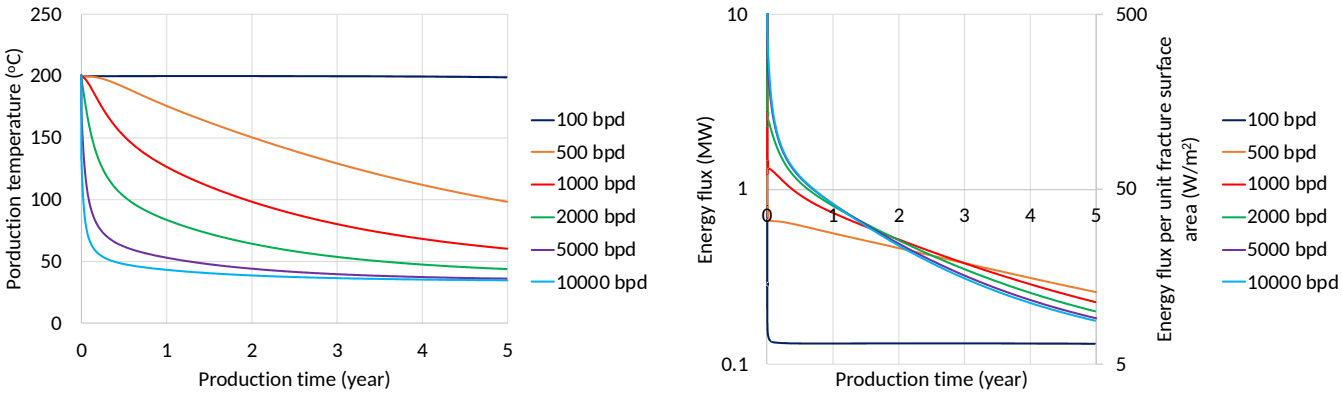

a **b**

Figure 13. Effect of injection rate. **a.** The temperature at the production well versus time. **b.** The net energy flux per fracture (left y axis) and net energy flux per unit fracture surface area (right y axis) at the production well versus time.

The results in the Figure 13(a) show that for a low injection rate (100 bpd per fracture) the production temperature remains almost constant. This means that the injected water is fully heated up by conduction while it travels through the fracture. However, the energy flux for this injection rate is barely above 0.1 MW per fracture. This indicates that the geothermal resource is not being utilized effectively. For higher injection rates (2000, 5000, and 10000 bpd), the production temperature drops below $50\,°C$, and although this provides a high initial energy flux, the energy flux drops sharply with time. In addition, if the produced water temperature is not high enough (e.g., below $100\,°C$), it is difficult to use the produced fluid for power generation. It could, however, be used for direct heating purposes. For an intermediate injection rate (500 bpd), the production temperature remains above $100\,°C$ for a five-year operation time. This may be a good injection rate to use if the produced fluids are to be used for power generation using steam turbines. This example illustrates the importance of using simulations to design EGS wells and fractures and use such results to optimize injection rates.

7.2 Effect of fracture spacing

In the second set of parametric runs, we investigate the effect of fracture spacing on enhanced geothermal systems. In the Base Case, the fracture spacing is 20 meters. Three more cases with fracture spacings of 10, 40, and 100 meters were run. The 100 meter case can also approximate a vertical well case (one hydraulic fracture per well) because of the large fracture spacing. The size of the reservoir domain and discretization have been adjusted accordingly to increase/decrease the size of the reservoir domain while keeping a constant grid size. All other parameters are kept the same as the Base Case.

The production temperature versus time for different fracture spacings is plotted in Figure 14(a). The net energy flux versus time for different fracture spacings is plotted in Figure 14(b). The net energy flux per unit fracture surface area is also plotted in Figure 14(b). Because in this set of runs, the fracture surface area for different cases is the same ($20000\,m^2$), the curves for net energy flux versus time and net energy flux per unit fracture surface area versus time overlap. For all fracture spacings, the production temperature and energy flux decrease and follow the

same trend for the first 5 months. During this time the temperature decrease has not reached the outer boundary for any of the cases. Once the outer boundary is reached, the production temperature and energy flux decrease dramatically for small fracture spacing. This is a direct consequence of the smaller energy content in the rock for the smaller fracture spacing. At late time, the injected water cannot be heated up effectively by the reservoir for the small fracture spacing cases. The 40-meter case and 100-meter case show very small differences in the production temperature within the five-year production duration, indicating that in these cases the temperature reduction front has not yet reached the boundary.

a

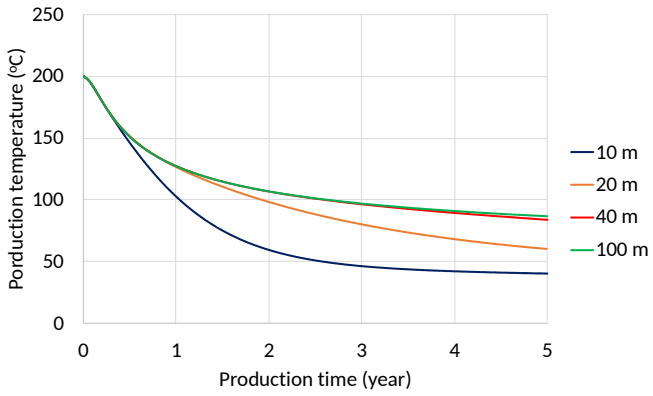

b

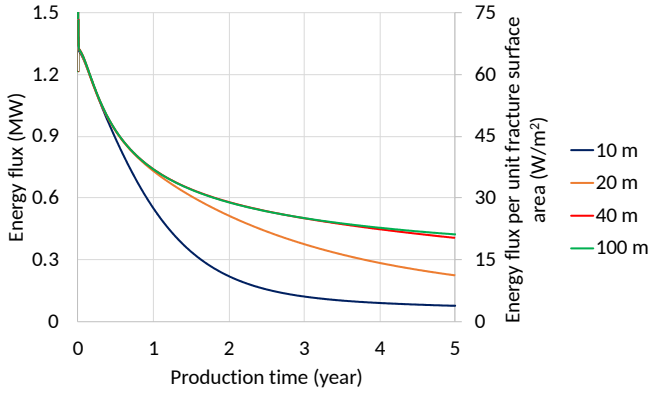

c

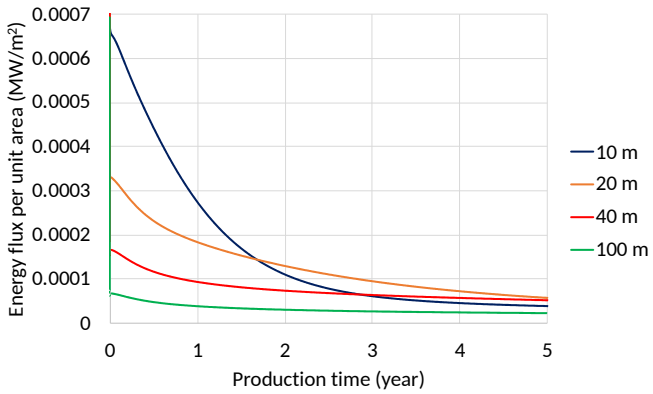

Figure 14. Effect of fracture spacing. **a.** The temperature at the production well versus time. **b.** The net energy flux per fracture (left y axis) and net energy flux per unit fracture surface area (right y axis) at the production well versus time. **c.** The net energy flux per unit land area at the production well versus time.

We plot the net energy flux per unit area versus time in Figure 14(c) to further investigate the efficiency of geothermal energy utilization under different fracture spacing. The area that the well and a single fracture occupy on the surface (well spacing times fracture spacing) for the four cases are 2000, 4000, 8000 and 20000 m^2. Although 10-meter and 20-meter fracture spacing cases have a higher heat recovery rate, the production temperature drops too fast in these two cases, making them less favorable for geothermal power generation. The 40-meter case doubles the energy flux per unit area compared to the 100-meter case while maintaining almost the same production temperature and energy flux, indicating a much higher energy extraction efficiency than the 100-meter case. This also indicates that horizontal wells with multiple hydraulic fractures are much more efficient at extracting heat from the reservoir than vertical wells with a single fracture in enhanced geothermal systems.

7.3 Effect of well spacing

In this section we examine the effect of well spacing. The well spacing in the Base Case is set to 200 meters. In this study, three more simulations are run with the well spacing set to 100, 300, and 400 meters. All other input parameters are maintained the same as the Base Case.

Figure 15(a) shows the production temperature versus time for the four cases. A larger well spacing gives a slower temperature decrease with time. This is because larger well spacing results in a longer contact time of the injected water with the rock and enables more heat transfer. Figure 15(b) shows the energy flux versus time and it follows the same trend as the production temperature. Figure 15(c) shows the energy flux per unit area of land. It also shows the energy flux per unit fracture surface area. The curves on the left y axis and right y axis overlap with each other because the unit area of land is proportional to the unit fracture surface area in this set of simulations. The area that the well and a single fracture occupy on the surface (well spacing times fracture spacing) for the four cases are 2000, 4000, 6000, and 8000 m^2. From Figure 15(c) one can see that the energy flux per unit area is very different in the first one and half years of operation, because reservoirs with a large well spacing design will be cooled down slower in the production well direction. After the first one and half years, the energy flux per unit area does not vary too much for different well spacings. This indicates that a larger well spacing design may be helpful to achieve a stable heat supply for a longer time. However, larger well spacing does make the hydraulic fracture design challenging in terms of achieving uniformly growing and propped fractures that connect the injection wellbore to the production wellbore.

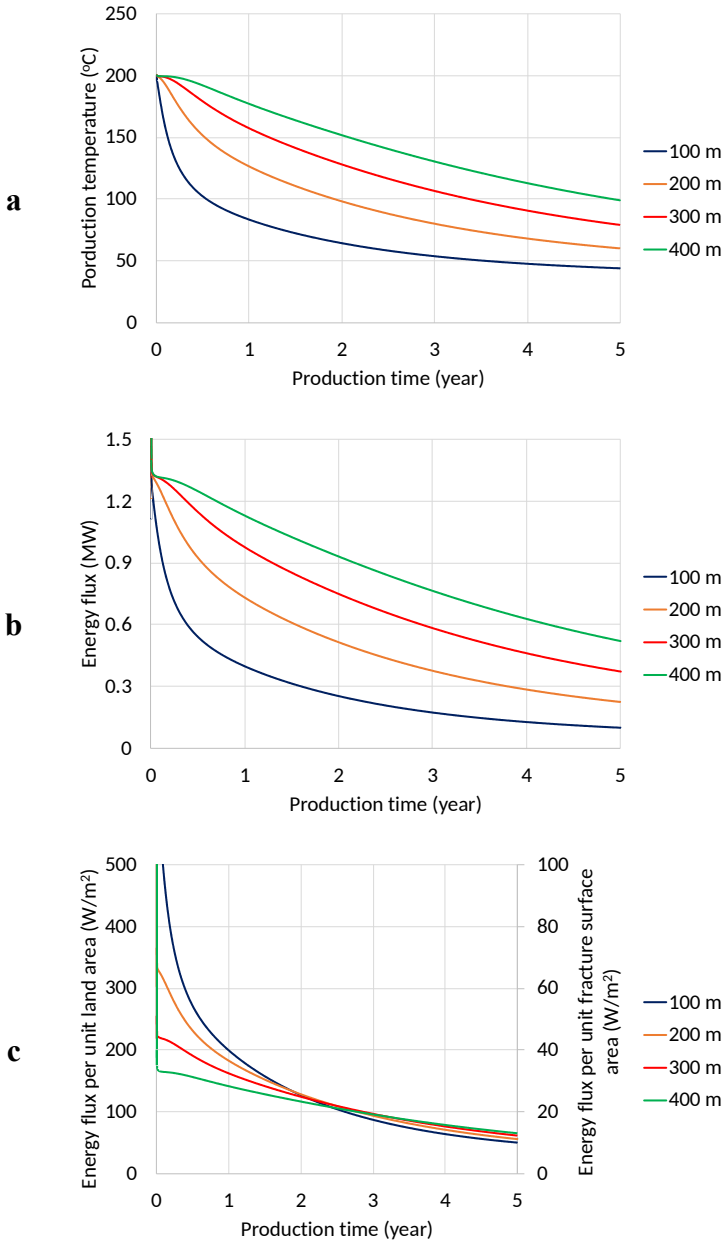

Figure 15. Effect of well spacing. **a.** The temperature at the production well versus time. **b.** The net energy flux per fracture, at the production well versus time. **c.** The net energy flux per unit land area (left y axis) and the net energy flux per unit fracture surface area (right y axis) at the production well versus time.

7.4 Effect of rock permeability

To investigate the effect of rock permeability we vary the rock permeability in the simulations from 1×10^{-16}, 1×10^{-17},1×10^{-18} (Base Case), and $1\times10^{-19}\,m^2$ while keeping other input parameters consistent with the Base Case. The production temperature and energy flux versus time for different permeability are plotted in Figure 16(a) and Figure 16(b). The results

only show very small differences at early time for different rock permeability. This observation can be explained by the fact that the initial changes in flux are related to the changes in fluid flow rate as the flow is initiated in the injector and producer. It should be noted that the simulations take into account gravity or pressure induced convection in the reservoir. However, in low permeability formations the rate of convection induced by gravity or by pressure gradients is very small. Increasing the permeability of the rock matrix can result in a large amount of fluid leak-off which would be undesirable if the fluid needs to be recirculated from the injection to the production well.

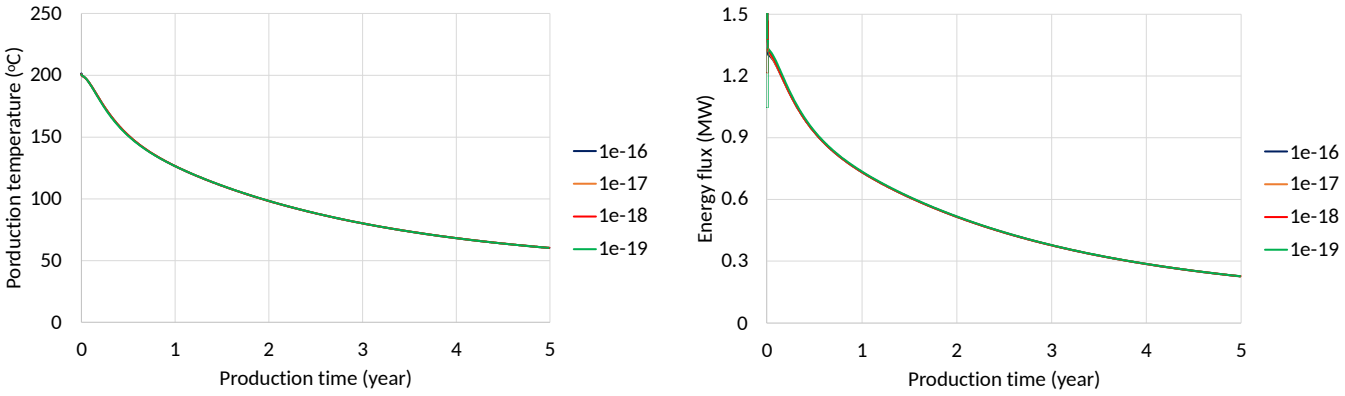

a **b**

Figure 16. Effect of reservoir permeability. **a.** The temperature at the production well versus time. **b.** The net energy flux per fracture at the production well versus time.

7.5 Effect of thermal boundary conditions

Boundary conditions can play a role in controlling the heat fluxes and temperature profiles at long injection times in enhanced geothermal systems. Typical geothermal gradients in the earth range from $10\,°C/km$ to $100\,°C/km$ (Lowell et al., 2014). We run three simulations with the thermal boundary condition at the bottom boundary of the sector model set to a fixed temperature of $200\,°C$, a fixed geothermal gradient of $10\,°C/km$, and fixed geothermal gradient of $100\,°C/km$. Fixing the temperature at the bottom boundary or setting temperature gradient at the bottom boundary defines a heat flux at the bottom boundary. This allows the EGS volume to be continuously re-supplied with geothermal energy from below.

The production temperature and energy flux versus time are shown in Figure 17(a) and Figure 17(b), respectively. The results show no significant differences from the no-flux boundary condition in the five years of production. This is because the heat flux from the earth (the bottom boundary) occurs by conduction, which is a very slow process. The difference will be small but become more apparent if the simulation time is longer (e.g., 10 years or 15 years). The time scale and rate of heat flux from the earth is much slower than the rate of heat extraction by fluid recirculation for a typical range of geothermal gradients.

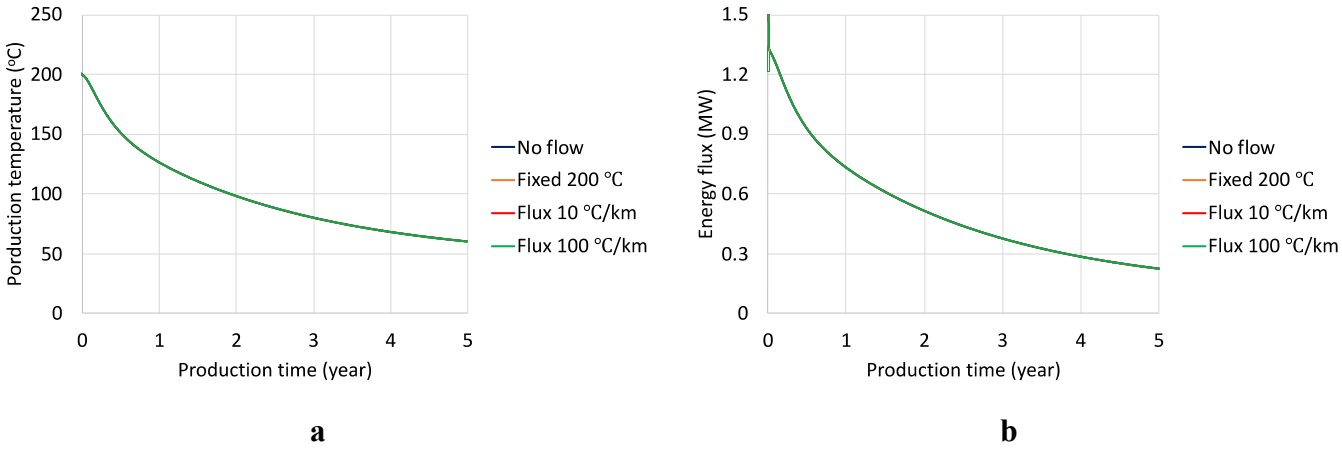

a **b**

Figure 17. Effect of thermal boundary condition at the bottom of the simulation domain. **a.** The temperature at the production well versus time. **b.** The net energy flux at the production well versus time.

7.6 Effect of non-uniform fluid injection

In all previous cases we assumed that each fracture created in the injection and production well are identical and planar. This results in a uniform distribution of injected fluid into each fracture in a horizontal well that may have more than 100 hydraulic fractures. This is clearly a simplifying assumption that allows us to study the impact of parameters that were discussed above. If, however, we relax this assumption and explore a more complicated case in which the distribution of the injected fluids is non-uniform, the performance of the system can be very different. To illustrate this effect, three cases are setup with two fractures included in the sector model.

1) In the first case, two fractures with uniform fracture width and permeability are included in the sector model (Figure 9(b)). The fracture spacing and fracture length are set to 20 meters and 200 meters. All other parameters are the same as the Base Case.
2) In the second case, one fracture is set to be the same as the fracture in the Base Case whereas the other fracture is assumed to have a length of 100 meters and a height of 30 meters, but it fails to connect to the production wellbore (Figure 9(c)).
3) In the third case, the two fractures are set to have different fracture surface area (Figure 9(d)). One fracture is set to be the same as the fracture in the Base Case whereas the other fracture is set to have a height of 30 meters.

In all the cases, the injection rate used is 1000 barrel per day for the sector (with two fractures). The production temperature and net energy flux for the three cases are shown in Figure 18(a) and Figure 18(b). The results clearly show that the failed connection case gives the fastest production temperature and energy flux decrease because only the fracture to the left contributes to the effective fracture surface area and the disconnected shorter fracture cannot contribute to heat extraction. In this circumstance, the reservoir rock in the right part of the sector cannot contribute as much heat energy as the reservoir rock in the left part of the sector, where the injector and producer are connected successfully by the fracture. The case in which fractures

have different surface area gives the second lowest production temperature and energy flux, which is caused by its lower fracture surface area. The case with the largest fracture surface area gives the highest production temperature and energy extraction rate, owing to its high fracture surface area among the cases. The energy extraction rate divided by the area of the connected fractures is shown in Figure 18(c). The heat content in the reservoir is the same for the three cases whereas the connected fracture surface areas are different. The failed connection case shows the highest energy extraction rate per unit fracture area because it has the smallest connected fracture surface area ($20000\,m^2$) and the highest fluid injection rate. The uniform case shows the lowest energy extraction rate per unit fracture area because it has the smallest connected fracture surface area ($40000\,m^2$). However, at late production time, the difference becomes small and the three curves converge.

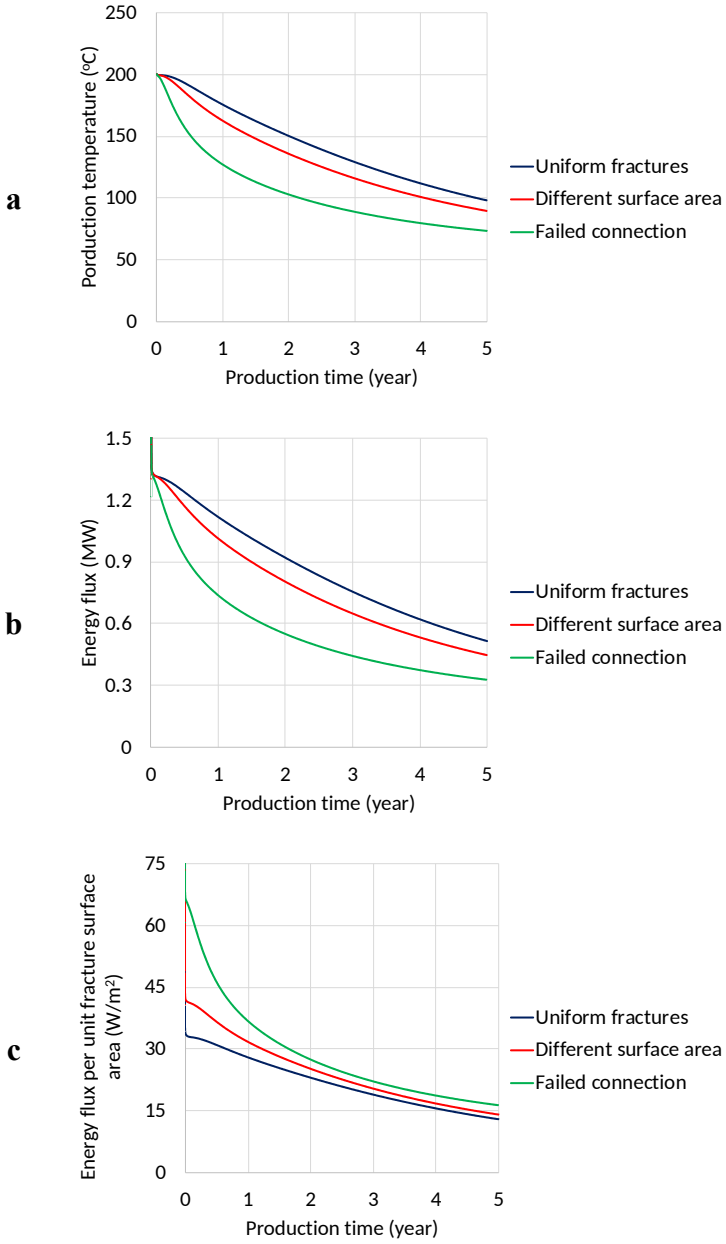

Figure 18. Effect of non-uniform fluid distribution among multiple fractures. **a.** The temperature at the production well versus time. **b.** The net energy flux at the production well versus time. **c.** The net energy flux per unit fracture area at the production well versus time.

8 Conclusions

In this paper, a single-component, water-steam two-phase geothermal reservoir simulation tool is presented. Coupled mass conservation-pressure-enthalpy equations are solved in the coupled reservoir/fracture domains using the p-h formulation. Both an implicit pressure, explicit enthalpy algorithm and a fully implicit algorithm have been developed. This simulator is validated with analytical solutions for one-dimensional and radial thermal flow problems. It is then used to study the key parameters affecting enhanced geothermal systems. It is shown that during the operation of an enhanced geothermal system, the temperature of the produced fluids and net energy flux decrease as energy is extracted from the reservoir. Based on our parametric study, it is found that injection rate, fracture spacing, well spacing, and effective (or connected) fracture surface area have the biggest impact on the heat extraction rate from the geothermal reservoir. It is also found that since most target reservoirs are ultra-low permeability, heat conduction is the main driver for heat flux in enhanced geothermal systems. Reservoir permeability does affect convective heat transport and may play a role when the rates of gravity driven convection are high. This is unlikely to be the case in most target reservoirs since this would imply very high leak-off rates in such high permeability reservoirs, making it very difficult to circulate fluids through the system. The outer thermal boundary condition may not affect short-term production from EGS but can be an important factor for long-term EGS development. For any given geothermal reservoir, an optimized EGS development plan can be designed using the geothermal reservoir simulator presented in this paper. Such simulators are an essential and efficient tool to optimize the fracture spacing, well spacing and injection rate in the geothermal reservoir development plan.

Acknowledgments

The authors acknowledge the Hydraulic Fracturing and Sand Control Industrial Affiliates Program at The University of Texas at Austin for the financial support.

Data Availability Statement

All data for the research comes from model simulations. The model description and implementation are discussed in Section 2, 3, and 4. The input parameters to the model are listed in Table 1, 2, and 3.

Nomenclature

d_v	Mass transfer term between the water and steam phase	kg/s
D	Depth	m^3
g	Gravity constant	m/s^2
h_i	Specific enthalpy of phase *i*	J/kg
h_{ss}	Specific enthalpy of saturated steam phase	J/kg
h_{ws}	Specific enthalpy of saturated water phase	J/kg

k	Matrix or fracture permeability	m^2
k_i	Thermal conductivity of phase *i*	$W \cdot m^{-1} \cdot K^{-1}$
k_{ri}	Relative permeability of phase *i*	
k_{rs}	Relative permeability of steam phase	
k_{rw}	Relative permeability of water phase	
k_s	Thermal conductivity of solid (rock)	$W \cdot m^{-1} \cdot K^{-1}$
K	Bulk thermal conductivity	$W \cdot m^{-1} \cdot K^{-1}$
p	Pressure	Pa
q_i	Volumetric source term of phase *i*	m^3/s
q_s	Volumetric source term for steam	m^3/s
q_w	Volumetric source term for water	m^3/s
S_i	Saturation of phase *i*	
S_s	Steam saturation	
S_w	Water saturation	
u_i	Darcy velocity of phase *i*	m/s
u_s	Darcy velocity of steam phase	m/s
u_w	Darcy velocity of water phase	m/s
U_r	Specific internal energy of the rock	J/kg
U_i	Specific internal energy of phase *i*	J/kg
V	Cell volume	m^3
μ_i	Viscosity of phase *i*	$Pa \cdot s$
μ_s	Viscosity of the steam phase	$Pa \cdot s$
μ_w	Viscosity of the water phase	$Pa \cdot s$
ρ_i	Density of phase *i*	kg/m^3
ρ_r	Density of the rock	kg/m^3
ρ_s	Steam density	kg/m^3
ρ_w	Water density	kg/m^3
ϕ	Porosity	

References

Baker, C.G. & Heroux, M.A. (2012). Tpetra, and the Use of Generic Programming in Scientific Computing. *Scientific Programming*, 20(2), pp.115-128. https://doi.org/10.3233/SPR-2012-0349

Bavier, E., Hoemmen, M., Rajamanickam, S. & Thornquist, H. (2012). Amesos2 and Belos: Direct and Iterative Solvers for Large Sparse Linear Systems. *Scientific Programming*, 20. https://doi.org/10.3233/SPR-2012-0352

Coats, K.H. (1977). *Geothermal reservoir modelling*. Paper presented at SPE Annual Fall Technical Conference and Exhibition. Society of Petroleum Engineers. https://doi.org/10.2118/6892-MS

Donaldson, I.G. & Sorey, M.L. (1979). *The best uses of numerical simulators*. Paper presented at fifth workshop on geothermal reservoir engineering, Stanford University, Stanford, California (Vol. 241).

Faust, C.R. & Mercer, J.W. (1979). Geothermal reservoir simulation: 1. Mathematical models for liquid−and vapor−dominated hydrothermal systems. *Water resources research*, 15(1), pp.23-30. https://doi.org/10.1029/WR015i001p00023

Faust, C.R. & Mercer, J.W. (1979). Geothermal reservoir simulation: 2. Numerical solution techniques for liquid−and vapor−dominated hydrothermal systems. *Water Resources Research*, 15(1), pp.31-46. https://doi.org/10.1029/WR015i001p00031

Heroux, M.A. (2004). *AztecOO user guide* (No. SAND2004-3796). Sandia National Laboratories.

Kennedy, B.M., Pruess, K., Lippmann, M.J., Majer, E.L., Rose, P.E., Adams, M., Roberston-Tait, A., Moller, N., Weare, J., Clutter, T. & Brown, D.W. (2010). *A History of Geothermal Energy Research and Development in the United States. Reservoir Engineering 1976-2006*. Office of Energy Efficiency and Renewable Energy (EERE), Washington, DC (United States). https://doi.org/10.2172/1218859

Lowell, R.P., Kolandaivelu, K. & P.A. Rona (2014). *Hydrothermal Activity, Reference Module in Earth Systems and Environmental Sciences*. Elsevier, ISBN 9780124095489. https://doi.org/10.1016/B978-0-12-409548-9.09132-6.

Mercer Jr, J.W. & Pinder, G.F. (1973). Galerkin finite-element simulation of a geothermal reservoir. *Geothermics*, 2(3-4), pp.81-89. https://doi.org/10.1016/0375-6505(73)90011-4

O'Sullivan, M.J., 1981. A similarity method for geothermal well test analysis. *Water Resources Research*, 17(2), pp.390-398. https://doi.org/10.1029/WR017i002p00390

Prokopenko, A., Siefert, C., Hu, J.J., Hoemmen, M.F. & Klinvex, A.M. (2016). *Ifpack2 User's Guide 1.0* (No. SAND2016-5338). Sandia National Lab. (SNL-NM), Albuquerque, NM (United States). https://doi.org/10.2172/1259544

Ross, B., Mercer, J.W., Thomas, S.D. & Lester, B.H. (1982). *Benchmark problems for repository siting models* (No. NUREG/CR--3097). GeoTrans.

Weller, H.G., Tabor, G., Jasak, H. & Fureby, C. (1998). A tensorial approach to computational continuum mechanics using object-oriented techniques. *Computers in physics*, 12(6), pp.620-631. https://doi.org/10.1063/1.168744

Wong, Z.Y. (2018). *Sequential-Implicit Newton's Method for Geothermal Reservoir Simulation* (Doctoral dissertation). Stanford University.

Zheng, S., Hwang, J., Manchanda, R. & Sharma M.M. (2020). An Integrated Model for Multi-Phase Flow, Geomechanics and Fracture Propagation. *Journal of Petroleum Science and Engineering*. https://doi.org/10.1016/j.petrol.2020.107716

Zheng, S., Manchanda, R. & Sharma, M.M. (2019). Development of a fully implicit 3-D geomechanical fracture simulator. *Journal of Petroleum Science and Engineering*, 179, pp.758-775. https://doi.org/10.1016/j.petrol.2019.04.065

Zheng, S. & Sharma, M.M. (2020). *Use of Stranded Natural Gas as a Fracturing Fluid: A Simulation Study*. Paper presented at Unconventional Resources Technology Conference. Society of Petroleum Engineers. https://doi.org/10.15530/urtec-2020-3233

Appendix A

In Appendix A, the Newton-Raphson formulation for fully implicit geothermal reservoir simulation is provided. In the p-h formulation, the pressure equation and the enthalpy equation are solved. Pressure and specific enthalpy are the primary unknowns. Section A.1. discusses the

finite volume and finite area discretization for the pressure and enthalpy equations. Section A.2. discusses the Newton-Raphson formulation.

A.1 Finite Volume Discretization

A.1.1 Pressure equation

Applying finite volume integration, the pressure equation in the reservoir domain becomes,

$$\sum_{i=1}^{2}\int_{V}\frac{\partial(\phi S_i\rho_i)}{\partial t}dV-\sum_{i=1}^{2}\int_{V}\nabla\cdot\left[\rho_i\frac{k\,k_{ri}}{\mu_i}\nabla(p-\rho_i gD)\right]dV-\sum_{i=1}^{2}\int_{V}\frac{\rho_i q_i}{V}dV=0$$

Applying the Gauss theorem, the integral equation becomes,

$$\sum_{i=1}^{2}\int_{V}\frac{\partial(\phi S_i\rho_i)}{\partial t}dV-\sum_{i=1}^{2}\oint_{S}n\cdot\left[\rho_i\frac{k\,k_{ri}}{\mu_i}\nabla(p-\rho_i gD)\right]dS-\sum_{i=1}^{2}\int_{V}\frac{\rho_i q_i}{V}dV=0$$

In an algebraic form, the equation can be expressed as,

$$\sum_{i=1}^{2}\frac{\partial(\phi S_i\rho_i)}{\partial t}V-\sum_{i=1}^{2}\sum_{f}\rho_i\frac{k\,k_{ri}}{\mu_i}\frac{\partial(p-\rho_i gD)}{\partial n}S_f-\sum_{i=1}^{2}\rho_i q_i=0$$

A.1.2 Enthalpy equation

Applying finite volume integration, the enthalpy equation in the reservoir domain becomes,

$$\int_{V}\frac{\partial}{\partial t}\left[(1-\phi)\rho_r h_r\right]dV+\sum_{i=1}^{2}\int_{V}\frac{\partial(\phi\rho_i h_i S_i)}{\partial t}dV-\int_{V}\nabla\cdot(K\nabla T)dV-\sum_{i=1}^{2}\int_{V}\nabla\cdot\left[\rho_i h_i\frac{k\,k_{ri}}{\mu_i}\nabla(p-\rho_i gD)\right]dV-\sum_{i=1}^{2}\int_{V}$$

Applying the Gauss theorem, the integral equation becomes,

$$\int_{V}\frac{\partial}{\partial t}\left[(1-\phi)\rho_r h_r\right]dV+\sum_{i=1}^{2}\int_{V}\frac{\partial(\phi\rho_i h_i S_i)}{\partial t}dV-\oint_{S}n\cdot(K\nabla T)dS-\sum_{i=1}^{2}\oint_{S}n\cdot\left[\rho_i h_i\frac{k\,k_{ri}}{\mu_i}\nabla(p-\rho_i gD)\right]dS-\sum_{i=1}^{2}\int_{V}\frac{\rho}{}$$

In an algebraic form, the equation can be expressed as,

$$\frac{\partial}{\partial t}\left[(1-\phi)\rho_r h_r\right]V+\sum_{i=1}^{2}\frac{\partial(\phi\rho_i h_i S_i)}{\partial t}V-\sum_{f}K\frac{\partial T}{\partial n}S_f-\sum_{i=1}^{2}\sum_{f}\rho_i h_i\frac{k\,k_{ri}}{\mu_i}\frac{\partial(p-\rho_i gD)}{\partial n}S_f-\sum_{i=1}^{2}\rho_i q_i h_i=0$$

A.2 Newton-Raphson Formulation for Reservoir Domain

In the p-h formulation, pressure and specific enthalpy are two independent variables. Other variables are all a function of the pressure and/or enthalpy. The following properties are functions of pressure and/or enthalpy: $\rho_w(p,h)$, $\rho_s(p,h)$, $S_w(p,h)$, $S_s(p,h)$, $h_w(p,h)$, $h_s(p,h)$, $h_{ws}(p)$, $h_{ss}(p)$, $\mu_w(p,h)$, $\mu_s(p,h)$, $k_{rw}(p,h)$, $k_{rs}(p,h)$, $K(p,h)$, $\phi(p,h)$, $T(p,h)$.

A.2.1 Pressure equation

Let the residual of the pressure equation be,

$$f_p=\sum_{i=1}^{2}\frac{\partial(\phi S_i\rho_i)}{\partial t}V-\sum_{i=1}^{2}\sum_{f}\rho_i\frac{k\,k_{ri}}{\mu_i}\frac{\partial(p-\rho_i gD)}{\partial n}S_f-\sum_{i=1}^{2}\rho_i q_i$$

Then the partial derivative of the pressure equation with respect to the pressure can be expressed as,

$$\frac{\partial f_p}{\partial p}=\sum_{i=1}^{2}\frac{V}{\Delta t}\left(S_i\rho_i\frac{\partial\phi}{\partial p}+\phi\rho_i\frac{\partial S_i}{\partial p}+\phi S_i\frac{\partial\rho_i}{\partial p}\right)-\sum_{i=1}^{2}\sum_{f}\frac{\partial\rho_i}{\partial p}\frac{kk_{ri}}{\mu_i}\frac{\partial\left(p-\rho_i gD\right)}{\partial n}S_f-\sum_{i=1}^{2}\sum_{f}\rho_i\frac{k}{\mu_i}\frac{\partial k_{ri}}{\partial p}\frac{\partial\left(p-\rho_i gD\right)}{\partial n}$$

The partial derivative of the pressure equation with respect to the enthalpy can be expressed as,

$$\frac{\partial f_p}{\partial h}=\sum_{i=1}^{2}\frac{V}{\Delta t}\left(\phi\rho_i\frac{\partial S_i}{\partial h}+\phi S_i\frac{\partial\rho_i}{\partial h}\right)-\sum_{i=1}^{2}\sum_{f}\frac{\partial\rho_i}{\partial h}\frac{kk_{ri}}{\mu_i}\frac{\partial\left(p-\rho_i gD\right)}{\partial n}S_f-\sum_{i=1}^{2}\sum_{f}\rho_i\frac{k}{\mu_i}\frac{\partial k_{ri}}{\partial h}\frac{\partial\left(p-\rho_i gD\right)}{\partial n}S_f+\sum_{i=1}^{2}\sum$$

A.2.2 Enthalpy equation

Let the residual of the enthalpy equation be,

$$f_h=\frac{\partial}{\partial t}\left[(1-\phi)\rho_r h_r\right]V+\sum_{i=1}^{2}\frac{\partial\left(\phi\rho_i h_i S_i\right)}{\partial t}V-\sum_{f}K\frac{\partial T}{\partial n}S_f-\sum_{i=1}^{2}\sum_{f}\rho_i h_i\frac{kk_{ri}}{\mu_i}\frac{\partial\left(p-\rho_i gD\right)}{\partial n}S_f-\sum_{i=1}^{2}\rho_i q_i h_i$$

Then the partial derivative of the enthalpy equation with respect to the pressure can be expressed as,

$$\frac{\partial f_h}{\partial p}=\frac{V\rho_r}{\Delta t}\left[-h_r\frac{\partial\phi}{\partial p}+(1-\phi)C_{pr}\frac{\partial T}{\partial p}\right]+\sum_{i=1}^{2}\frac{V}{\Delta t}\left(\rho_i h_i S_i\frac{\partial\phi}{\partial p}+\phi h_i S_i\frac{\partial\rho_i}{\partial p}+\phi\rho_i S_i\frac{\partial h_i}{\partial p}+\phi\rho_i h_i\frac{\partial S_i}{\partial p}\right)-\sum_{f}\frac{\partial K}{\partial p}\frac{\partial T}{\partial n}S$$

The partial derivative of the enthalpy equation with respect to the enthalpy can be expressed as,

$$\frac{\partial f_h}{\partial h}=\frac{V\rho_r}{\Delta t}(1-\phi)C_{pr}\frac{\partial T}{\partial h}+\sum_{i=1}^{2}\frac{V}{\Delta t}\left(\phi h_i S_i\frac{\partial\rho_i}{\partial h}+\phi\rho_i h_i\frac{\partial S_i}{\partial h}\right)-\sum_{f}\frac{\partial K}{\partial h}\frac{\partial T}{\partial n}S_f-\sum_{f}K\frac{\partial}{\partial n}\left(\frac{\partial T}{\partial h}\right)S_f-\sum_{i=1}^{2}\sum_{f}\frac{\partial\rho_i}{\partial h}h$$